Chapter 6

Structure, Local Structure driven Magnetic Properties of $CoMn_2O_4$ doped with Cr

6.1 Introduction

In this chapter, we investigate the crystal structure, local structure, and magnetic properties of $CoMn_{2-x}Cr_xO_4$ after doping with two different Cr concentrations (x = 0.50 and 1.00). A structural phase transition from the dominating tetragonal phase (space group: $I41/amd$) for x = 0.50 to pure cubic phase (space group: $Fd\bar{3}m$) is observed when x increases to 1.00 as discussed in section 6.2. Local structure examined through the XAFS spectra indicates that, while Co prefers A site, Mn and Cr prefer to occupy the B site, for both samples. From SEM, the particles are found to be of the micrometer size having a polygon shape. In section 6.3, magnetic characterization and analysis are discussed. Two magnetic transition temperatures for x = 0.50 and a single magnetic transition for x = 1.00 are also observed. Vertical magnetization shift with exchange bias is discussed in section 6.4. The results of this chapter are concluded in section 6.5.

6.2 Structure and microstructure

6.2.1 X-ray diffraction for Structural Analysis

For structural analysis, XRD measurement has been performed for $CoMn_{3-x}Cr_xO_4$ (x = 0.5 and 1.00). The diffraction pattern for x = 0.50, are well match with the JCPDS card no. 77-0471 and 23–1237 supporting the coexistence of tetragonal and cubic phases. While the diffraction pattern for x = 1.00 matches well with the cubic phase of JCPDS card no. 23–1237. To determine structural parameters, Rietveld refinement of XRD patterns for all the samples using FullProf suite choosing pseudo-voigt as a peak profile

function has been carried out. Space groups, $I41/amd$ and $Fd\bar{3}m$ are used for the tetragonal and cubic phases, respectively. The distribution of cations is chosen based on octahedral site preference energy (OSPE) and findings from published literature [80,161]. As per the above refinement condition, for the best fitting, χ^2 is found to be minimum i.e., between 1 to 2 for both the compositions. The Rietveld refinement pattern for x = 0.5 and 1.00 are shown in **Figure 6.1,** and refined parameters are tabulated in **Table 6.1**. Lattice parameters and cell volume for x = 0.50 are found to be a = b = 5.7905(4) Å, c = 8.8902(7) Å, and 298 Å^3, respectively, for tetragonal phase and a = b = c = 8.378(3)Å and 588 Å^3 for cubic phase. For x = 1.00, the lattice parameter and cell volume are found to be a = b = c = 8.36939(8)Å and 586.2482 Å^3.

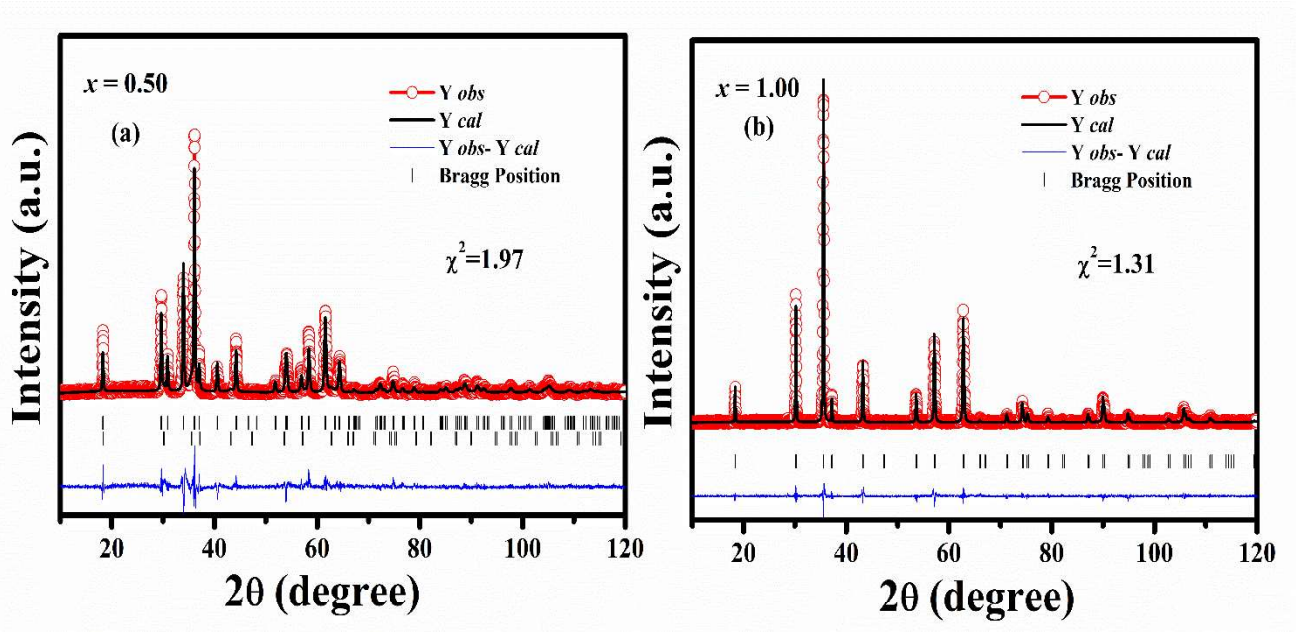

Figure 6.1: Experimental XRD pattern fitted with Rietveld refinement of FullProf program along with the difference pattern between experimental and calculated one, for $Co_xMn_{2-x}Cr_xO_4$ (a) x = 0.50, (b) x = 1.00.

Table 6.1: Rietveld refinement parameters for $CoMn_{2-x}Cr_xO_4$ where x = 0.50 and 1.00**.**

Parameter	**x = 0.50**		**x = 1.00**
Phase	Tetragonal	Cubic	Cubic
Space group	$I41/amd$	$Fd\bar{3}m$	$Fd\bar{3}m$
a [Å]	5.7905(4)	8.378(3)	8.36939(8)
b [Å]	5.7905(4)	8.378(3)	8.36939(8)
c [Å]	8.8902(7)	8.378(3)	8.36939(8)
Vol [Å^3]	298.0875	588.0593	586.2482
Co/Mn (A site)	4b (0, 1/4, 3/8)	8a (1/8, 1/8, 1/8)	8a (1/8, 1/8, 1/8)
OccA/Co [%]	97	50	95
OccA/Mn [%]	3	50	5
Co/Mn [B site]	8c (0, 0, 0)	16d (1/2, 1/2, 1/2)	16d (1/2, 1/2, 1/2)
OccB/Co [%]	1.5	25	2.5
OccB/Mn [%]	73.5	50	47.5
OccB/Cr [%]	25	25	50
O	16h (0, y, z) x: 0 y: 0.5161(9) z: 0.2391(6)	32e (x, y, z) x: 0.241(4) y: 0.241(4) z: 0.241(4)	32e (x, y, z) x: 0.2589(3) y: 0.2589(3) z: 0.2589(3)
Phase fraction	89	11	100
χ^2	1.97		1.31

For x = 0.5, 89 % is of tetragonal phase and 11 % is of cubic phase, whereas a pure cubic phase is detected when x =1.00. Here it is important to mention that, for x = 0.50, the phase fraction for cubic phase is found to be approximately equal to that of obtained for $CoMn_2O_4$ (8 %) in our previous literature [179]. For $Co_xMn_{3-x}O_4$, it is reported that with an increase in x from 1.00 to 2.00, dominating tetragonal phase to pure cubic phase transition is observed due to the substitution of the J-T active Mn^{3+} by Co^{3+} [181]. A similar transition is obtained in the present case. In general, Mn^{3+} has high OSPE i.e., most of the Mn^{3+} will occupy B site. However, with increase in x, there is a decrease in Mn^{3+} ions at the B site which is primarily caused by the substitution of Mn^{3+} with Cr^{3+} [2]. It is reported that when the concentration of Mn^{3+} ions in B site exceeds 55-65 %, the tetragonal symmetry is observed due to the Jahn-Teller (J-T) distortion. However, if the Mn^{3+} content in B sites is lower, the tetragonal distortion will not be prominent and the structure attains a cubic symmetry[2,102,182,183]. In the present case, coexistence of both phases for x = 0.5, confirms the higher amount of Mn^{3+} (> 55 %) ions present in the B site than that of x = 1.00, where a pure cubic phase is observed indicating less Mn^{3+} ions in the B site. In accordance with this, the refined occupancy indicates the cation distribution $(Co_{0.97}Mn_{0.02})[Co_{0.03}Mn_{1.47}Cr_{0.5}]O_4$ and $(Co_{0.5}Mn_{0.5})[Co_{0.5}Mn_{1.00}Cr_{0.5}]O_4$ for tetragonal and cubic phase, respectively, for x = 0.50. For x = 1.00, the cation distribution are found to be $(Co_{0.95}Mn_{0.5})[Co_{0.5}Mn_{0.95}Cr_{1.0}]O_4$, similar to the work shown by Humbe et al. for spinel ferrites [152]. Hence, Mn is found to be less than 50% in the octahedral site for the cubic phase. This indicates that, although Co and Mn are distributed in both A and B sites, Co dominatingly occupies the A site by attaining a +2 oxidation state and Mn dominatingly occupies the B site by attaining a +3 oxidation state. The remaining Co and Mn occupy B and A sites, respectively, as Co^{3+} and Mn^{2+}. Apart from this, Cr occupies

B site as Cr^{3+}, for both samples. Further to determine the local geometry and fine structure of the sample, XAFS analysis is performed.

6.2.2 XAFS analysis for cation distribution

Figure. 6.2(a–c) shows the normalized X-ray absorption near edge spectroscopy (XANES) and the pre-edge features recorded at Co, Mn and Cr K-edges for $CoMn_{2-x}Cr_xO_4$ (0.50 and 1.00). Previous findings indicate that the intense pre-edge features are mainly detected for the absorbing atom occupying a non-centrosymmetric environment such as a tetrahedral site because of the sum of the significantly large electric dipole transition and a small electric quadrupole transition [143,168,169]. Centrosymmetric environment, like the B site, where the electric dipole transition is not feasible, the pre-edge peaks are typically less intense[142,143,168–170]. When the absorbing atom occupies A site, a high intense pre-edge is observed while for the absorbing atom occupying the B site, pre-edge is absent, or a broad low intense pre-edge is observed. Before the pre-edge feature is analyzed, the background of pre-edge peak is subtracted using a spline function that smoothly tracks the data points before and after the pre-edge peak. At Co K-edge, a high intense pre-edge is observed which indicates that Co atom dominatingly occupies A site **(Figure 6.2(a))**. Similar feature of pre-edge has been reported by Miyasaka et al. for $CoMn_2O_4$ and Co_3O_4 where the Co ions are considered to be in Co^{2+} and Co^{3+} [114]. In contrast to Miyasaka et al., Bai et al. report two pre-edges for Co in Co_3O_4 where the two pre-edges are observed with normal spinel structure [171]. A similar pre-edge feature observed for Co in other spinels indicates the presence of Co^{2+} and Co^{3+} [172–175]. In accordance with the literature, the pre-edge features support the presence of Co^{2+} and Co^{3+} in the present case. The overlapping of the pre-edge for both the sample indicates that there is no significant change in the oxidation state of the Co atom. In case of Mn K-edge, pre-edge with low intensity is observed indicating that Mn is dominatingly present

in the B site **(Figure 6.2(b))**. Single pre-edge with centroid at near 6540 eV is observed similar to that of the reported for $CoMn_2O_4$ and Mn_3O_4 [114]. In addition to this, materials like Hausmannite (Mn_3O_4), Braunite (Mn_6SiO_{12}) and Franklinite ($Zn_{0.61}Mn_{0.39}(Fe_{1.94}Mn_{0.06})O_4$) having tetrahedral and octahedral environment with Mn^{2+} and Mn^{3+}, respectively, show the same pre-edge features for Mn [104,165]. The same pre-edge feature observed for both the samples indicate that there is no change in the valencies of Mn for both the samples. **Figure 6.2(c)** shows approximately negligible pre-edge for both the samples at Cr K-edge indicating the strong preference of Cr at B site. Further to confirm the occupancy, fourier transform (FT) EXAFS spectra at Co, Cr, and Mn K-edges without phase corrections are depicted in **Figure 6.3(a-c)**. For the spinels, there are three common peaks (say I_o, I_B and I_A) that emerge near 1.5 Å, 2.5 Å, and 3.0 Å at Co, Cr and Mn K-edges in EXAFS spectra. Where, I_o is attributed to the interaction of absorber atom with its first nearest neighbour oxygen, I_B and I_A correspond to the cations present at the B and A sites, respectively [114,141]. At Co K-edge, the intensity of I_A peak is very high in comparison to I_B, confirming the dominance of Co in A site for both samples **(Figure 6.3(a))**. Whereas, increase in the intensity for x =1.00 indicates that with increase in Cr content Co is more prominent in A site. For Mn K-edge spectra, high intense I_B peak is observed, confirming the presence of Mn at B site for both the samples. For x = 1.00, I_B becomes sharp and highly intense, which may be due to the absence of J-T distortion in cubic phase and increment of Mn in B site in comparison to the tetragonal phase **(Figure 6.3(b))**. At Cr K-edge, intensity of I_B is very high in comparison to the intensity of I_A, confirming the presence of Cr at B site. Hence, in the present case, Co dominatingly occupies A site and, Cr and Mn dominatingly occupy the B site. With increase in the Cr content, Cr^{3+} replaces the Mn^{3+} at B site without significant disturbance in occupancy or oxidation state of the other atoms present at A site.

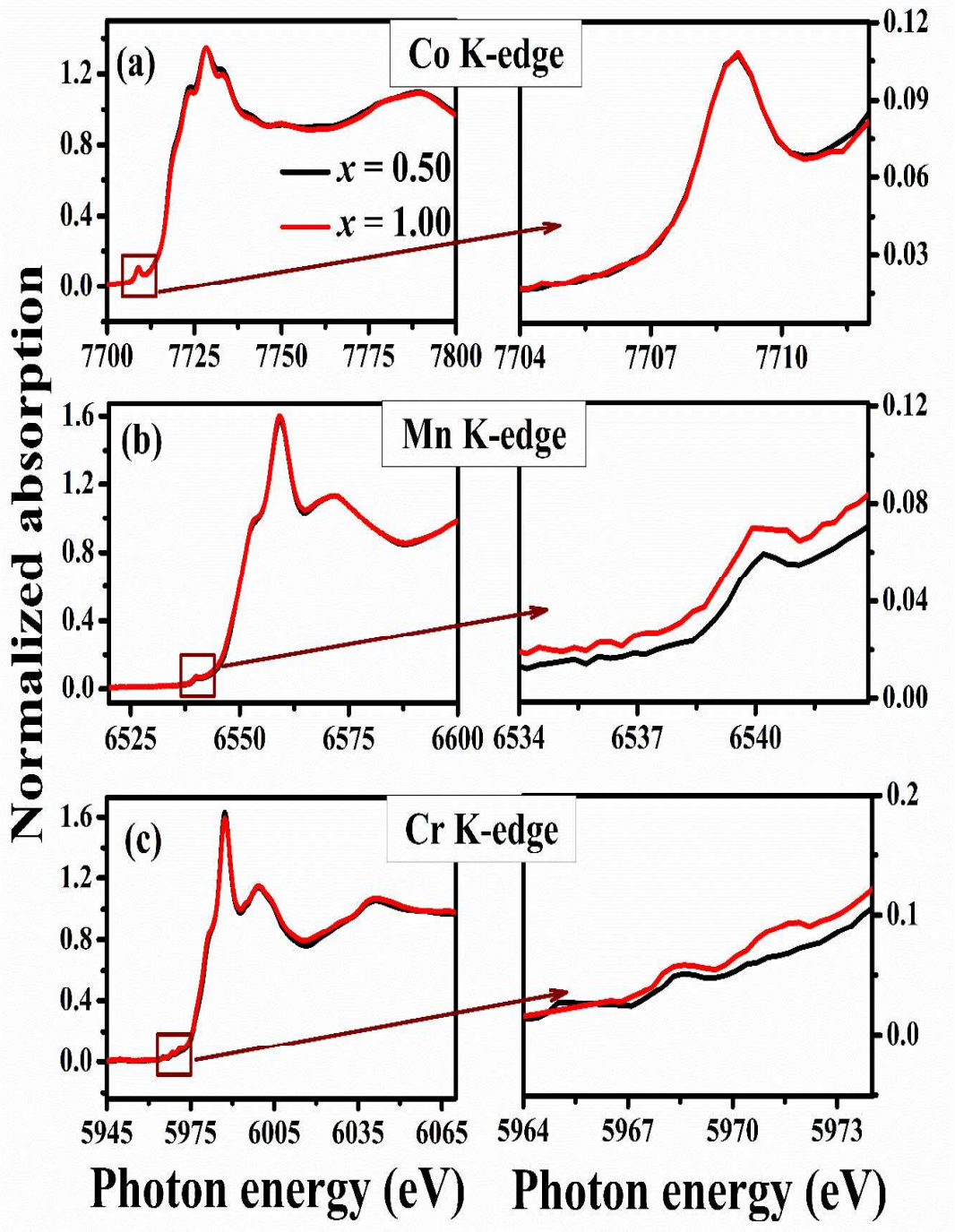

Figure 6.2: XANES spectra collected at the (a) Co K-edges with enlarged view of the corresponding pre-edge region (b) Mn K-edges with enlarged view of the corresponding pre-edge, and (c) Cr K-edges with enlarged view of the corresponding pre-edge.

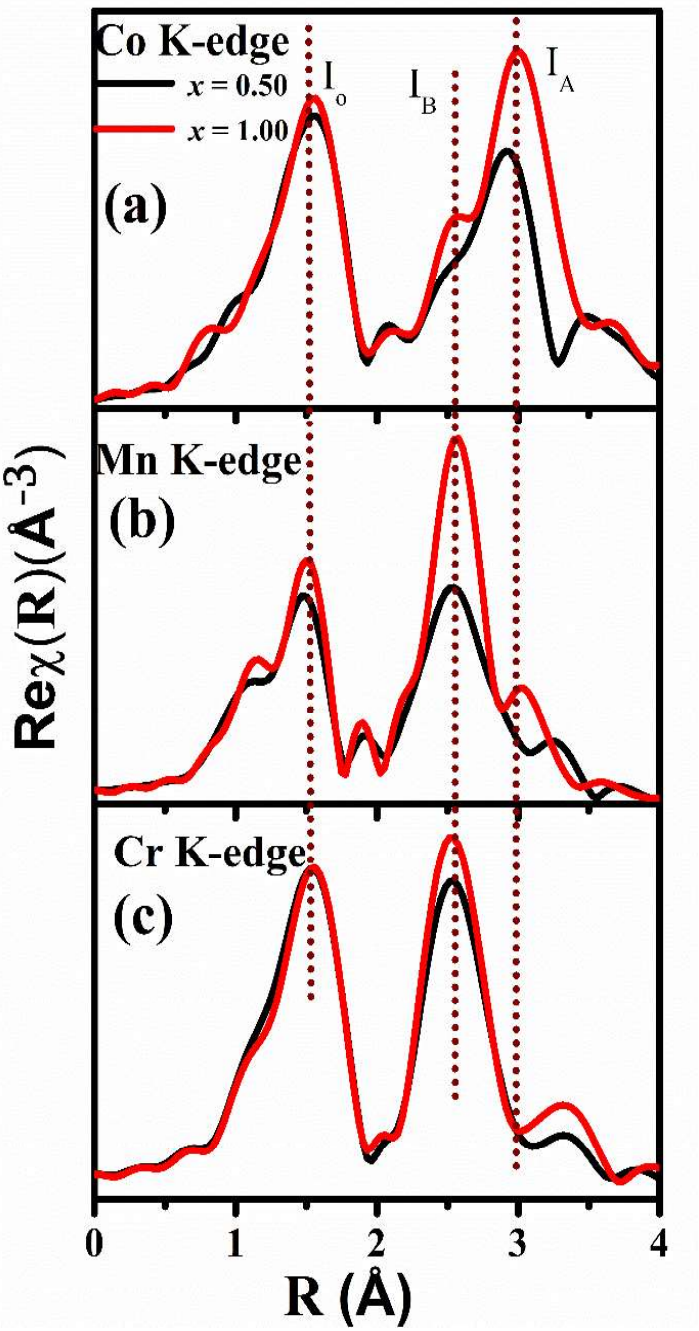

Figure 6.3: Fourier transforms magnitude of EXAFS spectra of (a) Co K-edge(b) Mn K-edge, and (c) Mn K-edge.

6.2.3 SEM Analysis for Morphology

Scanning electron micrographs depicted in **Figure 6.4(a, b, d, and e)**, show the spherical polygon shape for x = 0.50 and hexagonal shape for x = 1.00. From particle size distribution histogram, average particle size is found to be ~ 1.06 and 0.54 µm for x = 0.50 and 1.00 respectively as shown in **Figure 6.4(c and f)**. Further, the distribution and concentration of Mn, Cr, and Co are confirmed from the elemental mapping and energy dispersive X-ray spectroscopy (EDS) as shown in **Figure 6.5**. Elemental mapping shows that Mn, Cr and Co are homogeneously distributed and EDS analysis shows the Mn, Cr and Co ratio close to 1.50:0.50:1.00 and 1.00:1.00:1.00, as required in $CoMn_{1.5}Cr_{0.5}O_4$ and $CoMnCrO_4$ respectively. Thus, it is well corroborated with XRD results and confirms the stoichiometry of $CoMn_{2-x}Cr_xO_4$ particles.

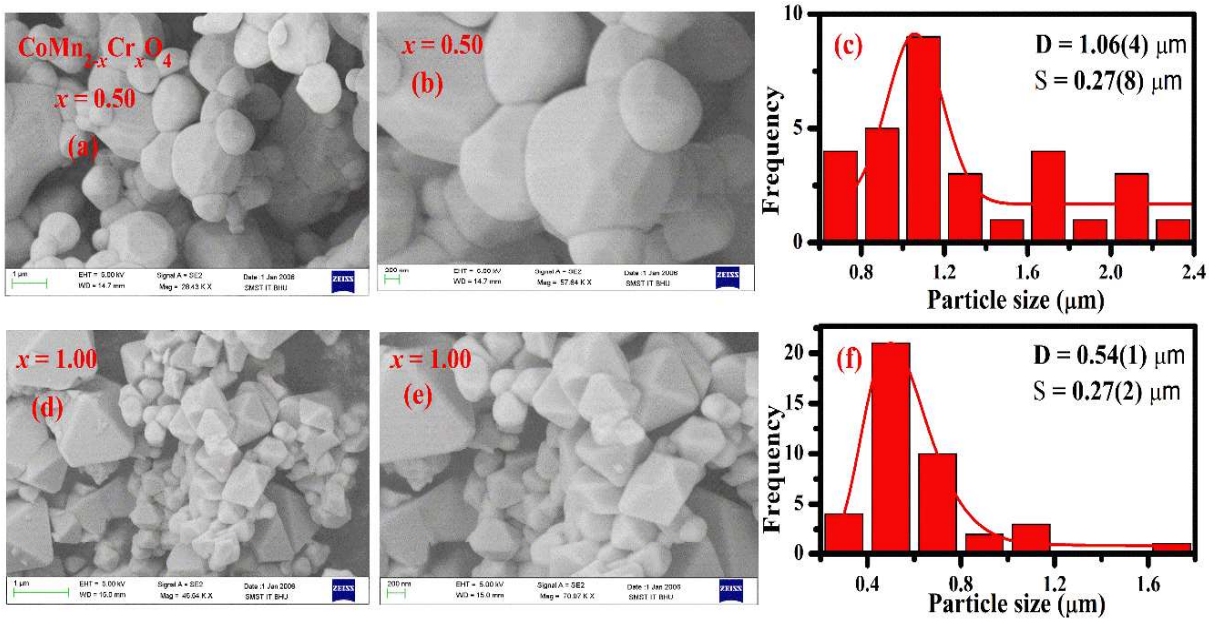

Figure 6.4: (a,b,d and e) SEM images, (c and f) particle size distribution histogram.

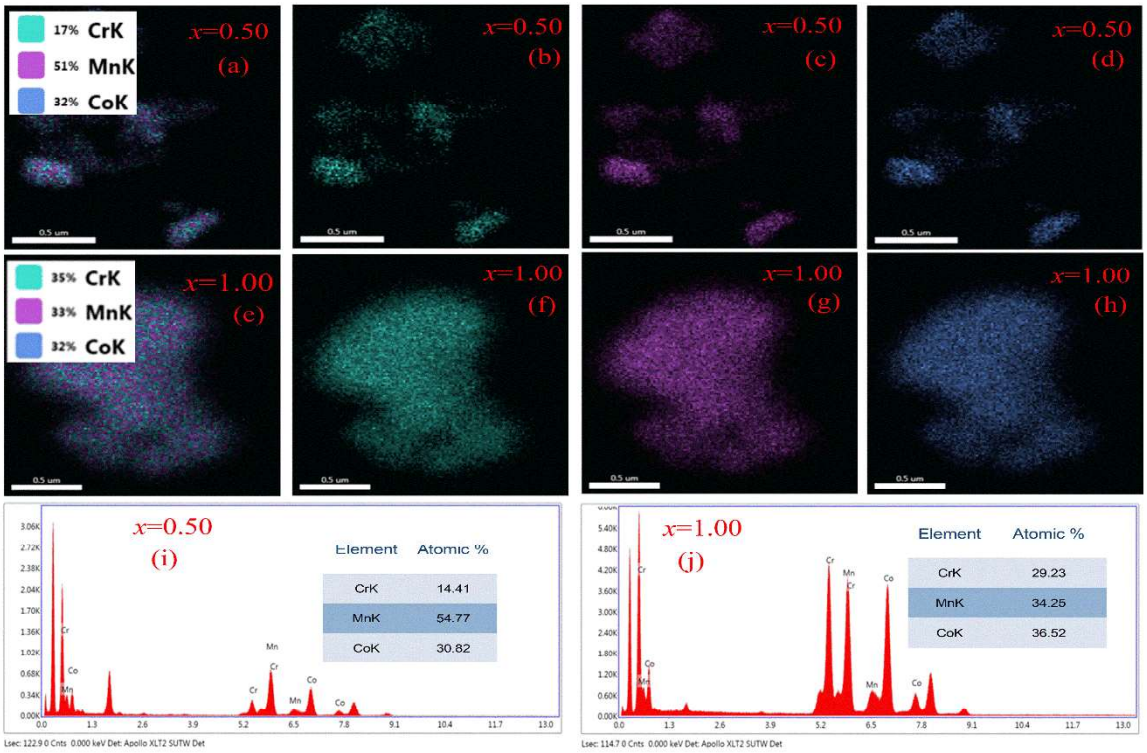

Figure 6.5: (a-h)Elemental mapping images(i and j) energy dispersive spectra.

6.3 Magnetic Analysis

6.3.1 Temperature dependent magnetization

Magnetization (M) of the $CoMn_{2-x}Cr_xO_4$ ($x = 0.5$ and 1.00) particles has been measured with varying temperature and magnetic field (H). The temperature dependent magnetization measured under zero field cooling (ZFC) and field cooling (FC) with an external magnetic field of 0.5 kOe in the temperature range of 3 to 300 K is depicted in **Figure 6.6(a, c)**. For x = 0.5, with decreasing temperature from 300 K, magnetization shows a peak, Tp_1 at 156 K and another peak Tp_2 at 101 K. Moreover, the transition temperature is determined at the point where the tangent to the magnetization peak intersects with the extrapolation of the paramagnetic line on the temperature axis **(Figure 6.6(b, d))**. Thus, the transition temperatures Tc_1 (169 K) and Tc_2 (110 K) are obtained

for x = 0.5, corresponding to the Tp_1 and Tp_2, respectively. On increasing x to 1.00, one may note that a single magnetic transition Tc_1 is revealed at 128 K with a magnetization peak Tp_1 at 121 K. These two transitions Tc_1 and Tc_2 have been reported in $CoMn_2O_4$ where Tc_1 is attributed to the presence of few impurity phases associated with $Co_xMn_{3-x}O_4$ and Tc_2 is due to the existence of Yafet–Kittel (Y-K) spin structure [83,103,122]. In Mn based spinels, for tetragonal structure, Y-K spin is attributed to non-collinear triangular spin canting arrangement arising due to the Mn^{3+} ions present in the B site, while ions in A site have collinear ferromagnetic behaviour [80,83]. However, in case of cubic structure, ions occupying the A and B site attain FM and AFM arrangement, respectively[49,161]. The competition between these ions among A and B site results in such magnetic transitions. Notably in x = 0.5, the tetragonal phase with a small fraction of cubic phase, shows that the magnetization peak corresponds to Tc_2 and small magnetization peak corresponds to Tc_1. However, x = 1.00 having pure cubic phase demonstrates only one magnetization peak corresponding to Tc_1. We have found similar results for $Co_xMn_{3-x}O_4$ (x = 1.00 to 2.00), where the intensity of Tp_1 and Tp_2 is found to be depend on the phase fraction of cubic and tetragonal phase respectively. Thus, in the present case, it is concluded that the magnetic transition corresponding to Tc_1 is ascribed to the cubic phase, while Tc_2 is attributed to the tetragonal phase. It is important to mention that with Cr doping, while Tc_1 is found to be decreased, Tc_2 is found to be increased in comparison to that of reported for $CoMn_2O_4$ [179]. Such changes are attributed to the Co and Mn interaction with Cr. Further, it is interesting to note that in the ZFC magnetization curve at low temperature, magnetization becomes negative. The observed negative magnetization while is negligible in case of x = 0.5, with an increase in x from 0.50 to 1.00, negative magnetization shows a significant increase **(Figure 6.6(b, d))**. Due to the presence of Cr, the magnetic moments of the two sublattices are unequal and also vary with temperature.

Thus, negative magnetization effect arises from the competition between two sublattices at different crystallographic sites where the magnetization of one sublattice is dominating on the other, similar to an earlier report on $Co(Cr_{1-x}Mn_x)_2O_4$ in the range of $0.3 \leq x \leq 0.5$ [116]. At T= 55.5 K, compensation of magnetization is observed for x = 1.00 **(Figure 6.6(b)).**

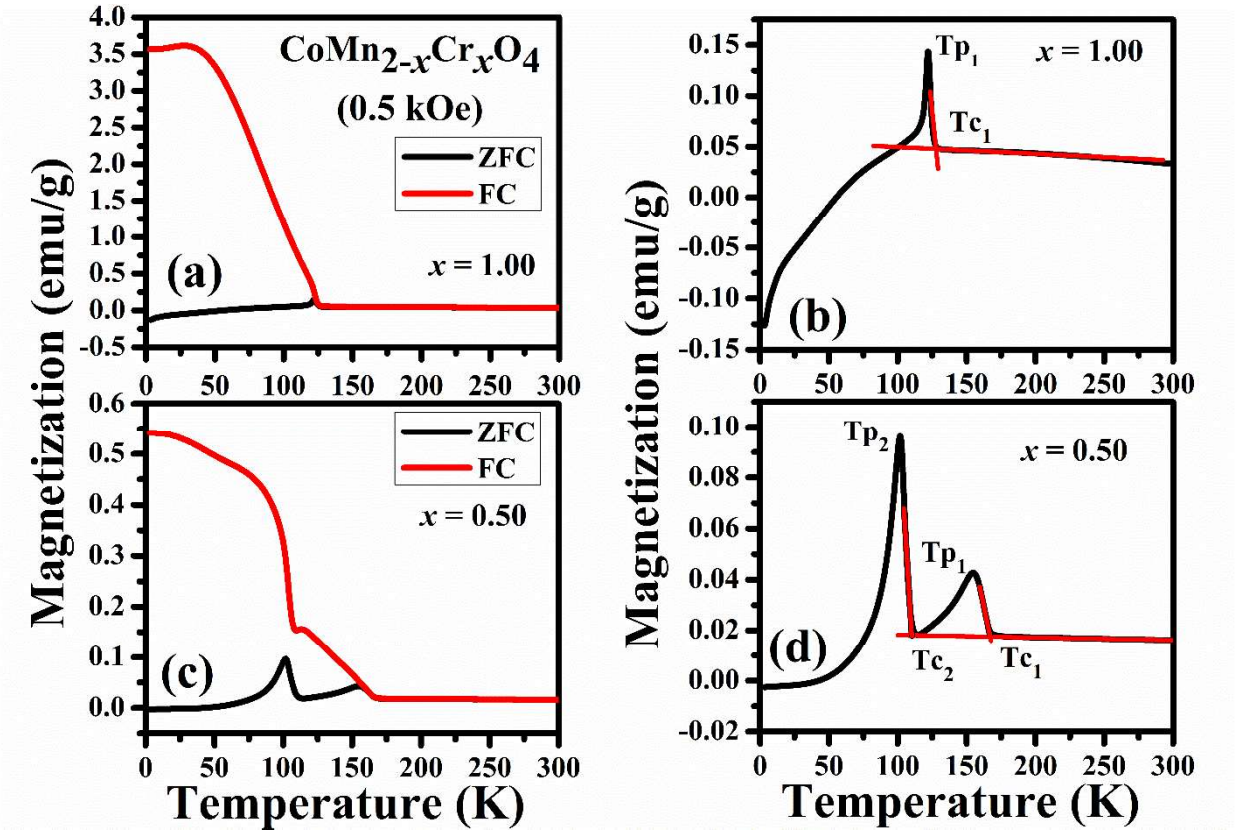

Figure 6.6: (a, and c) FC-ZFC magnetization versus temperature, (b and d) shows the enlarged view of peaks and transitions obtained in ZFC curve for x = 1.00 and 0.50 respectively.

To further explore the magnetic behaviour of x = 1.00, the ZFC and FC magnetization have been conducted at different field i.e. 0.5 to 10 kOe as shown in **Figure 6.7.** With increase in magnetic field, T_{irr} is found to be decreased from 126.6 K at 0.5 kOe to 114 K at 10 kOe. Interestingly, ZFC magnetization is found to increase with

increase in the magnetic field and not only become positive at lower temperature for 5000 Oe, but also shows a sudden increase with increase in the temperature. This behaviour can be explained based on the compensation of sublattice magnetization with applied external magnetic field and temperature. At low applied field and at low temperature, one sublattice dominates over the other and also does not allow to align the moment of that sublattice in the field direction. When the applied field increases, the moments are aligned in the field direction and magnetization becomes positive. The observed complex M-T behavior may significantly influence magnetization measurements under varying external magnetic fields across different temperatures.

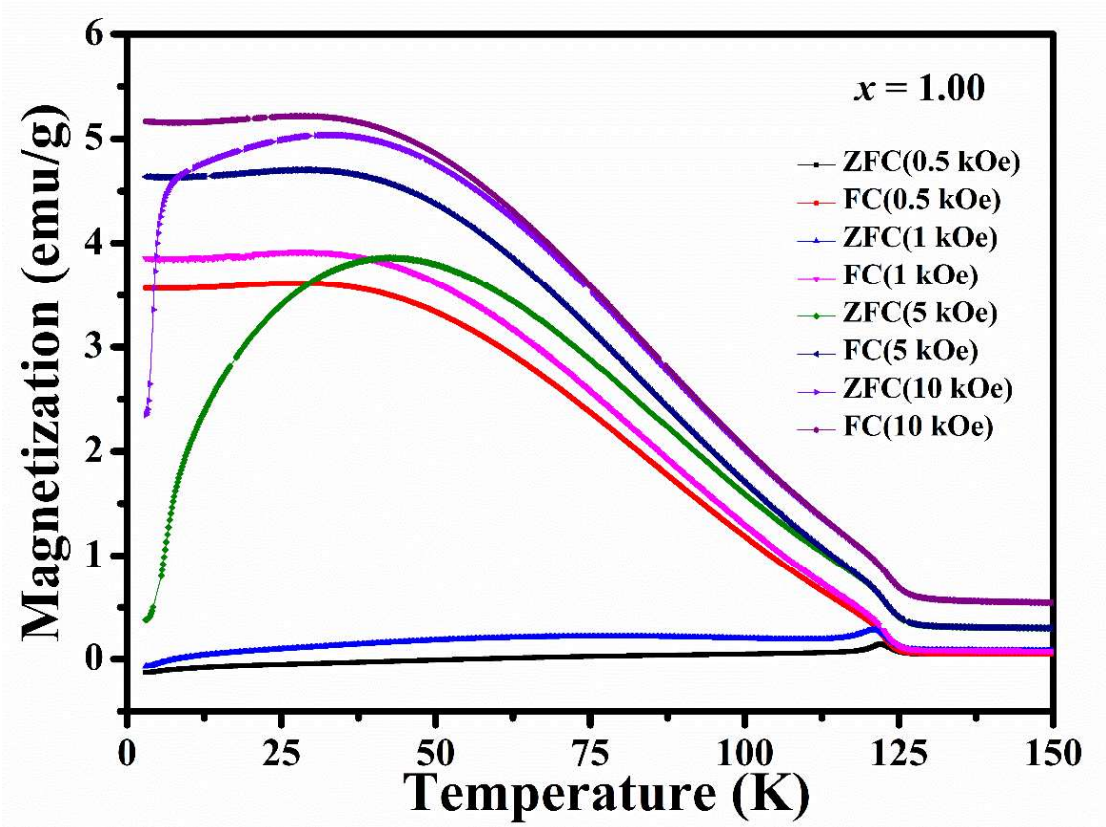

Figure 6.7: Temperature dependent (ZFC, lower branches; FC, upper branches) at 0.5, 1, 5 and 10 kOe.

6.3.2 Field dependent magnetization

Magnetization versus magnetic field curve in the magnetic field range of −60 to +60 kOe at different temperature for $CoMn_{2-x}Cr_xO_4$ (x = 0.50 and 1.00) are shown in **Figure 6.8(a, c)**. For x = 0.50, unsaturated hysteresis loop present at higher field for all temperatures, confirms a strong signature of spin canting effect[158–160], while for x = 1.00 approximately saturated loop is observed. At room temperature, magnetization shows a linear M-H behaviour with increase in field, confirming the paramagnetic nature for both samples. For x = 0.50, with decrease in the measuring temperature, the M-H loop area increases and become maximum at 50 K followed by a decrease, while for x = 1.00 M-H loop area continuously increases and becomes maximum at minimum measuring temperature i.e. at 5 K. Hc vs T curve are depicted in **Figure 6.8 (b and d),** for both samples. It may be noted that for x = 0.50, Hc is found to increase with a decrease in temperature and become maximum (5.171 kOe) at 50 K followed by a decrement. However, for x = 1.00, the general ferrimagnetic behaviour is observed. Hc is found to increase with decrease in temperature and shows a maximum of 6.464 kOe at 5 K. Here one may note that for x = 0.5, M_{ZFC} shows two transitions Tc_1 and Tc_2, while for x = 1.00 M_{ZFC} shows a single magnetic transition Tc_1. Following this, H_C shows temperature dependent behaviour as mentioned above. Thus, for x = 0.50, the decrement in Hc at lower temperature is related to the magnetic phase associated with the Tc_2 transition corresponding to the tetragonal phase. Hence, the decrease in Hc could be related to the Y-K spin structure associated with Mn^{3+} present in B site of tetragonal phase as depicted in chapter 5. In the present case the decrement of Hc at lower temperature is less compared to $CoMn_2O_4$, may be due to the replacement of Mn^{3+} by Cr^{3+} in B site of tetragonal phase.

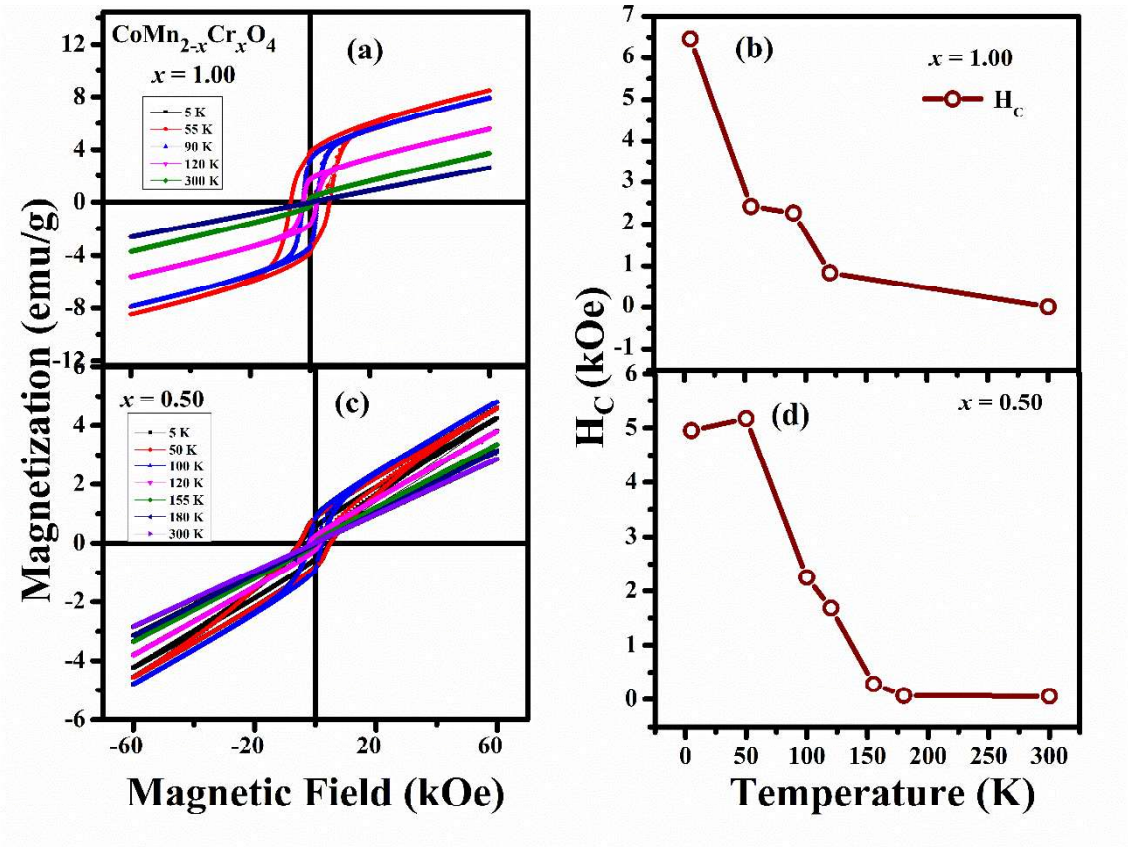

Figure 6.8: (a, and c) ZFC Magnetization vs magnetic field hysteresis loops, (b and d) Hc vs temperature at various measuring temperatures.

6.4 Exchange bias and VMS

As two sublattice magnetizations depend on temperature, one may expect the exchange bias to occur in these spinels also. Therefore, we measure the exchange bias by cooling the sample at 10 kOe from room temperature to the desired temperature and measuring the hysteresis behaviour. **Figure 6.9** indicates the M-H loops under zero field cooling (ZFC) and field cooling (FC) conditions, at 5 K for x = 0.50 and 1.00. Surprisingly for x = 0.5, FC hysteresis loops shift up in the magnetization (Y) axis (VMS) and shift left in magnetic field (X) axis, indicating the presence of vertical magnetization shift (VMS) and conventional exchange bias (H_{CEB}), respectively. However, for x = 1.00, the shifting is not observed confirming the absence of VMS and H_{CEB}. For x = 0.5, the high exchange bias of 3422 Oe obtained at 5 K which seems to be overestimated due to the non-

saturation of magnetization and high irreversibility in magnetization during the hysteresis cycle. To estimate the exact H_{CEB}, VMS is subtracted from the hysteresis loop to bring back the loop to the centre. With this correction, H_{CEB} is estimated and found to be 397 Oe at 5 K. To further clarify the VMS and exchange bias behaviour of x = 0.50, FC M-H is conducted at different temperature (5, 25, 50, 75 and 100 K) as depicted in **Figure 6.10 (a)**. Enlarged view of the loops are shown in **Figure 6.10 (b).** VMS is found to be decreased from 0.4 emu/g at 5 K to 0.00 emu/g at 100 K which is near Tp_2. With increase in temperature from 5 to 25 K, H_{CEB} is significantly decreased from 397 to 28 Oe, which is negligible at 50 K. This suggests that VMS and H_{CEB} have different origin as reported for $CoMn_2O_4$ in chapter 3 [179]. Thus, in the present case, similar to $CoMn_2O_4$[179,181], VMS is mainly decided by Mn^{3+} present in octahedral site which is associated with Y-K spin related with tetragonal structure, the conventional exchange bias originates from the interaction between differently arranged spins of the A and B sublattices which changes with temperature.

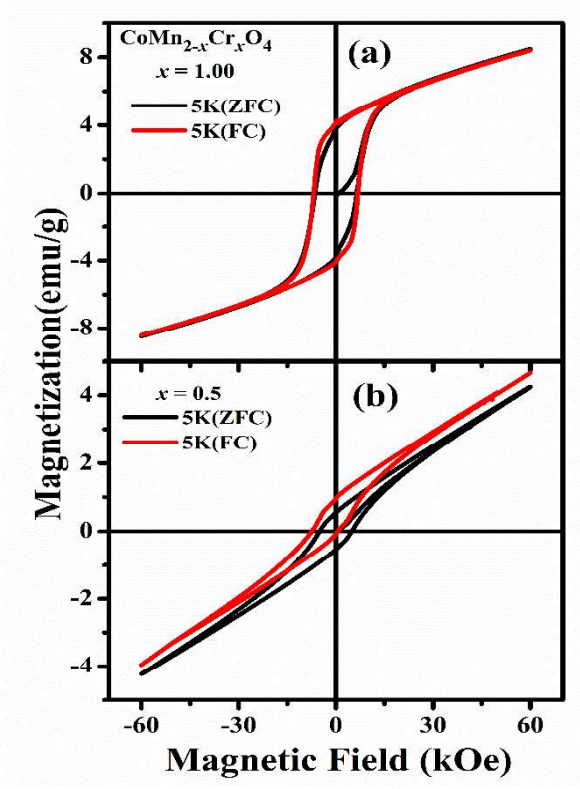

Figure 6.9: ZFC and FC M-H curve for, (a) x = 0.50, (b) x = 1 .00

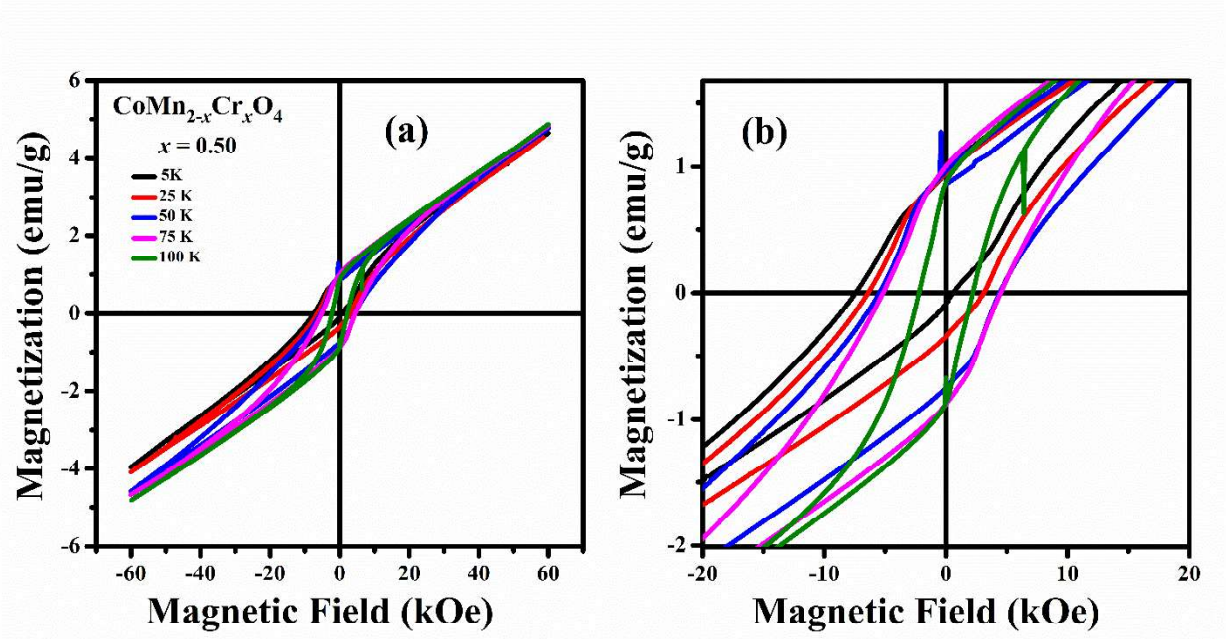

Figure 6.10: (a) FC M-H curve at different temperature (5,25,50,75, and 100K), and (b) enlarged view showing the loop shift.

6.5 Conclusion

Structural transformation from tetragonal to cubic phase was demonstrated when Cr doped in $CoMn_2O_4$. Rietveld refinement of $CoMn_{2-x}Cr_xO_4$ revealed transformation from coexistence of tetragonal and cubic phases having phase fractions 89% and 11% respectively, for $x = 0.50$, to a pure cubic phase for $x = 1.00$. This was associated with the substitution of Jahn-Teller active Mn^{3+} by Cr^{3+}. XAFS analysis confirmed that Co^{2+} ions dominantly occupied the A site, while Cr^{3+} and Mn^{3+} dominantly occupied the B site in both samples. Corresponding to the two structural phases, $x = 0.50$ exhibited two magnetic transitions (Tc_1 at 169 K and Tc_2 at 110 K), whereas $x = 1.00$ showed a single magnetic transition (Tc_1 at 128 K). Additionally, $x = 0.50$ showed a conventional exchange bias H_{CEB} of 397 Oe and a vertical magnetization shift (VMS) of 0.4 emu/g at 5 K. In contrast, H_{CEB} and VMS were absent for $x = 1.00$, for which negative magnetization was observed in ZFC M-T curve. The VMS, H_{CEB}, and negative

magnetization were explained by competition between the spin among A and B sublattices, where VMS was mainly decided by the presence of Mn^{3+} in the B sublattice.